Article | Open Access

Energy Materials

Yu *et al. Energy Mater.* **2026**, *6*, 600044 **DOI:**10.20517/energymater.2026.25

Asymmetric carbazole-based self-assembled monolayers enable simultaneous efficiency and stability enhancement in organic solar cells

Yangyang Yu[1], Xin Hong[2], Yuan Li[2], Zhengfei Wang[2], Feiyu Kang[2,*], Zhiwei Jiao[1,*], Guodan Wei[2,*]

Keywords:
Organic solar cells, self-assembled monolayer, asymmetric molecules, hole transport layer

Citation: Yu, Y.; Hong, X.; Li, Y.; Wang, Z.; Kang, F.; Jiao, Z.; Wei, G. Asymmetric carbazole-based self-assembled monolayers enable simultaneous efficiency and stability enhancement in organic solar cells. *Energy Mater.* **2026**, *6*, 600044. https://dx.doi.org/10.20517/energymater.2026.25

Received: 20 Feb 2026
First Decision: 12 Mar 2026
Revised: 28 Mar 2026
Accepted: 16 Apr 2026
Published: 6 May 2026

Academic Editor: Sining Yun
Copy Editor: Fangling Lan
Production Editor: Fangling Lan

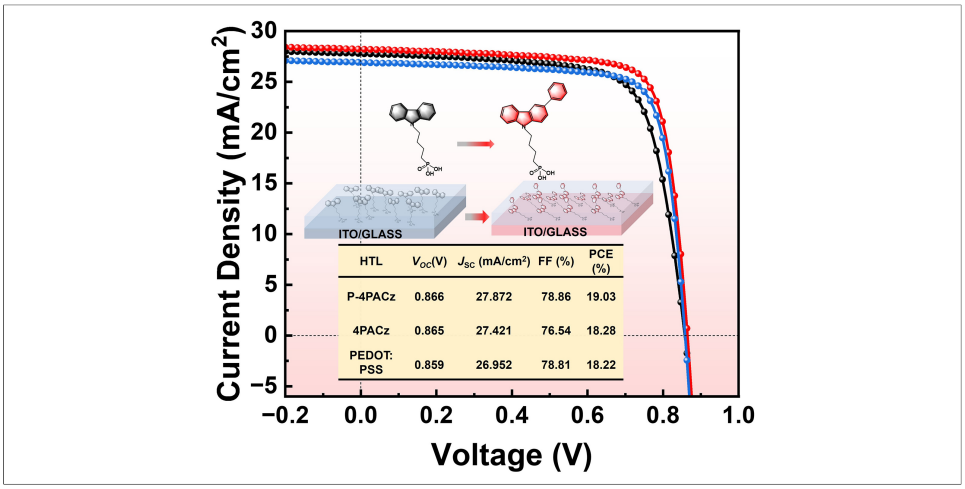

Abstract

Self-assembled monolayers (SAMs) have emerged as powerful interfacial modifiers for high-performance organic solar cells. Currently reported asymmetric substitution strategies have primarily focused on tuning molecular dipole moments and work functions or enhancing π-π stacking to improve interfacial quality. In contrast, our work reports an asymmetric carbazole-based SAM molecule, P-4PACz, featuring a unilateral phenyl substituent at the 3-position of the carbazole core. This asymmetric design alters the π-π stacking mode to a tightly packed yet slipped configuration, which enables ordered solid-state assembly while suppressing excessive pre-aggregation in solution. Such an approach enables a favorable balance between solution processability and interfacial ordering. Compared with its symmetric analogue 4PACz, P-4PACz exhibits reduced surface energy on indium tin oxide, improved energy-level alignment, and suppressed molecular aggregation, resulting in enhanced active-layer wetting and interfacial contact. This optimized interface promotes efficient hole extraction while mitigating interfacial recombination losses. Consequently, P-4PACz-based devices achieve a champion power conversion efficiency (PCE) of 19.03%, outperforming 4PACz (champion 18.28%) and

[1]College of Science, China Jiliang University, Hangzhou 310018, Zhejiang, China.
[2]Institute of Materials Research, Tsinghua Shenzhen International Graduate School, Tsinghua University, Shenzhen 518000, Guangdong, China.

*Correspondence to: Prof. Guodan Wei, Prof. Feiyu Kang, Institute of Materials Research, Tsinghua Shenzhen International Graduate School, Tsinghua University, Shenzhen 518000, Guangdong, China. E-mail: weiguodan@sz.tsinghua.edu.cn; fykang@sz.tsinghua.edu.cn; Prof. Zhiwei Jiao, College of Science, China Jiliang University, Hangzhou 310018, Zhejiang, China. E-mail: jzwgj@163.com

PEDOT:PSS (champion 18.22%) controls. The superiority of P-4PACz is further validated across multiple representative systems, including PM6:L8-BO (champion 18.16%), PM6:PY-DT (champion 16.35%), PM6:Y6 (champion 16.73%), demonstrating its broad applicability. In addition to enhanced efficiency, P-4PACz-based devices exhibit improved operational stability, retaining 80% of their initial PCE after 782 h of continuous illumination.

INTRODUCTION

Solution-processed organic solar cells (OSCs) are a promising green energy technology for achieving carbon neutrality due to their lightweight nature, mechanical flexibility, and compatibility with low-cost and large-area manufacturing processes[1-3]. Recent breakthroughs in non-fullerene acceptors and device engineering have enabled their PCEs[4-6]. However, high efficiency alone is insufficient for practical deployment; long-term operational stability remains a critical requirement. One of the major bottlenecks limiting OSC stability is the widely used hole transport layer (HTL), poly(3,4-ethylenedioxythiophene): polystyrene sulfonate (PEDOT:PSS)[7-9]. Although PEDOT:PSS enables high efficiency, it suffers from several intrinsic drawbacks. Its strong acidity corrodes indium tin oxide (ITO) electrodes and promotes In^{3+} diffusion into the photoactive layer, accelerating device degradation[10]. Moreover, its hygroscopic nature facilitates moisture and oxygen ingress, which exacerbates photo-oxidative instability. From an electronic perspective, the relatively high HOMO level of PEDOT:PSS leads to suboptimal energy-level alignment, limiting the achievable open-circuit voltage (V_{OC}). Additionally, parasitic absorption in the near-infrared region reduces photon flux reaching the active layer, constraining the short-circuit current density (J_{SC}). Collectively, these limitations compromise both the efficiency and long-term stability of OSCs, underscoring the urgent need for alternative HTLs that simultaneously provide high performance and enhanced durability.

Since 2018, SAMs have emerged as a highly promising class of HTLs for OSCs due to their molecular tunability, ultralow material consumption, and compatibility with solution processing. Their well-defined molecular structures enable precise control over interfacial energetics and charge-transport properties. Among them, carbazole-based phosphonic acid derivatives, particularly 2PACz, have achieved state-of-the-art device performance and established a benchmark for SAM-based HTLs[11-15]. To further optimize device performance, extensive molecular engineering strategies have been explored[16]. These include tuning alkyl-chain length to optimize packing and film formation[17], introducing methoxy groups to improve interfacial wettability[18], halogenation (e.g., F or Cl) to modulate HOMO levels and work-function alignment[19,20], and asymmetric substitution to tailor molecular dipoles and interfacial energetics[21,22]. More recently, extended asymmetric π-conjugated frameworks have been designed to enhance molecular ordering and facilitate interfacial charge transport[23-26]. However, practical translation to large-area OSCs requires not only improved interfacial properties but also structural simplicity, good solubility, and uniform film formation[27-33]. For example, 4PACz, an extended derivative of 2PACz, improves charge extraction through enhanced steric interactions but suffers from limited solubility and strong aggregation tendency, leading to non-uniform films and interfacial defects[34].

To address these challenges, we report an asymmetric SAM molecule, P-4PACz, featuring a phenyl substituent at the 3-position of the carbazole core. Different from other asymmetric strategies that rely on strengthening intermolecular π-π stacking or modifying charge distribution via halogen substitution, this asymmetric molecule is characterized by the following features: (1) it strategically modulates π-π stacking to mitigate common issues such as poor solubility and excessive pre-aggregation in solution; (2) it maintains appropriately balanced intermolecular interactions during assembly, enabling the formation of ordered self-assembled monolayers that further influence active layer morphology. This structural modification increases the molecular dipole moment from 2.08 to 2.19 D, strengthening phosphonic acid anchoring to the

ITO surface through combined steric and electronic effects. Simultaneously, the phenyl substituent suppresses pre-aggregation in solution via steric hindrance, enabling the formation of denser and more homogeneous SAM films[35]. As a result, P-4PACz creates smoother, lower-energy ITO surface, leading to improved active layer wetting and interfacial contact. Using P-4PACz as the HTL, bulk-heterojunction OSCs based on PM6:BTP-eC9 photoactive system exhibit enhanced hole extraction, suppressed bimolecular and trap-assisted recombination, and prolonged carrier lifetimes compared to devices employing symmetric 4PACz or PEDOT:PSS. Consequently, the champion P-4PACz-based device shows a PCE of 19.03%, outperforming symmetric 4PACz (champion 18.28%) and PEDOT:PSS (champion 18.22%) controls, and delivers the longest T_{80} lifetime of up to 782 h under controlled conditions (25 °C, 25% relative humidity, AM 1.5G illumination 100 mW/cm^2). These results demonstrate that asymmetric molecular engineering of SAM-based HTLs enables synergistic optimization of interfacial energetics, film morphology, and charge-transport dynamics. This strategy provides a practical pathway toward high-efficiency and stable OSCs compatible with scalable fabrication.

EXPERIMENTAL

Material synthesis

PM6, BTP-eC9, Y6, PY-DT, L8-BO and PNDIT-F3N were from Solarmer Materials Inc (Beijing), PEDOT:PSS (CLEVIOS™ P VP AI 4083) was purchased from Heraeus, 4PACz and P-4PACz (Beijing Green Guardee Technology), 1-Naphthyl chloride (1-CN) and 1,8-Diiodooctane (DIM) were purchased from TCI (Shanghai). The ITO-coated glass (≤ 15 Ω/square) was purchased from Advanced Election Technology. All reagents were purchased from Sigma-Aldrich and were used without further purification.

Device fabrication

Devices with the conventional ITO/HTL/active layer/PNDIT-F3N/Ag architecture were fabricated on commercial ITO glass. Substrates were sequentially ultrasonicated in DI water, IPA, acetone and IPA for 15 min each, dried under nitrogen and oxygen-plasma treated for 300 s to yield hydrophilic surfaces. Inside a nitrogen glovebox, SAM films (0.3 mg mL^{-1} in ethanol) were spin-coated at 3,000 rpm for 30 s, rested for 30 s and annealed at 85 °C for 10 min; when required, a PEDOT:PSS reference was deposited at 5000 rpm for 20 s and annealed at 150 °C for 10 min in air. Active layers were then spin-coated at 3,000 rpm for 30 s under the same inert atmosphere: PM6:BTP-eC9 and PM6:L8-BO were cast from 16 mg mL^{-1} chloroform (D:A 1:1.2 with 0.25 vol% DIM) and annealed at 95 and 90 °C for 5 min, respectively; PM6:Y6 was processed from 17 mg mL^{-1} chloroform (D:A 1:1.2, 0.5 vol% 1-CN) and annealed at 85 °C for 10 min; PM6:PY-DT was deposited from 16 mg mL^{-1} chloroform (D:A 1:1.25, 1.5 vol% 1-CN) and annealed at 100 °C for 10 min. The PNDIT-F3N was dissolved in methanol at a concentration of 0.5 mg mL^{-1} with 0.5 vol% acetic acid and was spin-coated onto the active layer at a speed of 3,000 rpm for 30 s, and 100 nm Ag electrodes were thermally evaporated through a shadow mask at 3 × 10^{-4} Pa to define an active area of 0.06 cm^2, completing the device.

Measurements and instruments

The ultraviolet-visible (UV-Vis) absorption spectra of the films were recorded on an HP 8453 spectrophotometer (Hewlett-Packard, USA). Single crystals of 4PACz and P-4PACz were grown via the vapor diffusion method. Sufficient powder of 4PACz or P-4PACz was dissolved in dichloromethane and transferred into a small vial. The small vial was then placed into a larger vial containing methanol, and the whole system was sealed and stored in a refrigerator. Suitable block-like single crystals for X-ray diffraction analysis were obtained after several days. Atomic force microscopy (AFM) imaging was performed in tapping mode using a Bruker Dimension Icon system (Bruker, USA). Conductive AFM (C-AFM) measurements were conducted on an Asylum Research Cypher AFM system (Oxford Instruments, UK). During these measurements, the sample was either illuminated or kept in the dark using a top-mounted integrated LED, while a bias voltage of -8.7 mV was applied between the conductive tip and the sample.

Kelvin probe force microscopy (KPFM) characterization was carried out on an Oxford Instruments Cypher ES system, employing a Ti/Ir-coated conductive cantilever to simultaneously acquire topographic and surface potential maps. X-ray photoelectron spectroscopy (XPS) data were acquired using a Kratos Axis Ultra Imaging XPS spectrometer (Kratos Analytical Ltd., UK) equipped with a 300 W Al Kα X-ray source. The base pressure during data acquisition was maintained at ~3 × 10^{-9} mbar. All binding energies were referenced to the C 1s peak of adventitious carbon at 284.8 eV. Ultraviolet photoelectron spectroscopy (UPS) measurements were performed using a He I radiation source (21.22 eV) on a Thermo Scientific GENESIS 500 system (Thermo Fisher Scientific, USA), with the sample biased at -10.0 V. Current density-voltage (*J-V*) characteristics were measured under simulated AM 1.5 G illumination (100 mW cm^{-2}) using a computer-controlled Keithley 2400 (Keithley Instruments, USA) source measurement unit coupled to a Newport Oriel solar simulator (Newport Corporation, USA). Light intensity was calibrated against a certified NREL silicon reference cell. External quantum efficiency (*EQE*) spectra were recorded using an Enlitech QE-R system (Enlitech, Taiwan, China) and calibrated with a certified single-crystal silicon reference cell. Steady-state photoluminescence (PL) spectra were recorded using an Edinburgh Instruments fluorescence spectrometer (Edinburgh Instruments, UK), with excitation provided by a Xe 900 xenon lamp and detection performed by an RP928 photomultiplier tube. All optical and electrical characterizations were carried out at room temperature (25 °C). Electrochemical impedance spectroscopy (EIS) measurements were conducted on the OSC devices using a CHI760E (Shanghai Chenhua, China) precision electrochemical impedance analyzer. All EIS measurements were performed under dark conditions. Impedance spectra probing recombination kinetics were acquired at V_{OC} over a frequency range of 10 MHz to 1 Hz, whereas spectra reflecting charge carrier transport properties were measured under zero applied bias across a frequency range of 10 MHz to 0.01 Hz. The built-in potential (V_{bi}) was determined via Mott-Schottky analysis from capacitance-voltage (C-V) measurements, which were performed under dark conditions across a voltage range of -0.2 to 1.0 V at a frequency of 10 kHz, using the standard relationship $1/C^2$ *vs.* V. The V_{bi} was extracted from the linear region of the $1/C^2$-V plot as the x-intercept. The light-intensity dependence of the V_{OC} was evaluated inside a nitrogen-filled glovebox under standard test conditions (AM 1.5G, 100 mW/cm^2). Illumination intensity was systematically varied from 0.3 to 100 mW/cm^2 using a calibrated silicon reference solar cell equipped with a KG5 filter and controlled via a Keithley 2400 source measure unit.

Photocurrent density (J_{ph}) and effective voltage (V_{eff}) were determined from current density-voltage curves in light and dark states with a high applied voltage from -1 to 3 V. J_{ph} is defined as $J_{ph} = J_{light} - J_{dark}$, where J_{light} and J_{dark} are the values of current density under the illumination of AM 1.5G, 100 mW/cm^2 and in dark, respectively. $V_{eff} = V_0 - V_{app}$, where V_0 refers to the voltage while $J_{light} = J_{dark}$, and V_{app} are the applied voltage. At a high effective voltage, all free charges in the film are completely expelled and gathered by the electrodes, a state that is temperature-independent and is referred to as the saturation current (J_{sat}).

RESULTS AND DISCUSSION

The molecular structures of P4PACz ((4-(3-phenyl-9H-carbazol-9-yl)butyl) phosphonic acid) and 4PACz ((4-(9H-carbazol-9-yl) butyl) phosphonic acid) are presented in Figure 1A. The key feature of this asymmetric modification lies in its subtle yet meaningful influence on the molecular dipole moment characteristics. Although the dipole moment orientation is altered [Figure 1B and Supplementary Figure 1], its magnitude increases only slightly from 2.08 to 2.19 D. Furthermore, the introduction of the phenyl substituent induces a redistribution of the electrostatic potential (ESP). Compared with symmetrical 4PACz, P-4PACz exhibits an expanded negative ESP region extending from the carbazole core toward the phenyl-substituted side, while the positive ESP remains primarily localized on the alkyl chain and phosphonic acid moiety. This spatial redistribution of charge density reflects the asymmetric electronic environment introduced by phenyl substitution [Figure 1C]. Density functional theory (DFT) calculations further reveal that the asymmetric phenyl group induces a downward shift of the Highest Occupied

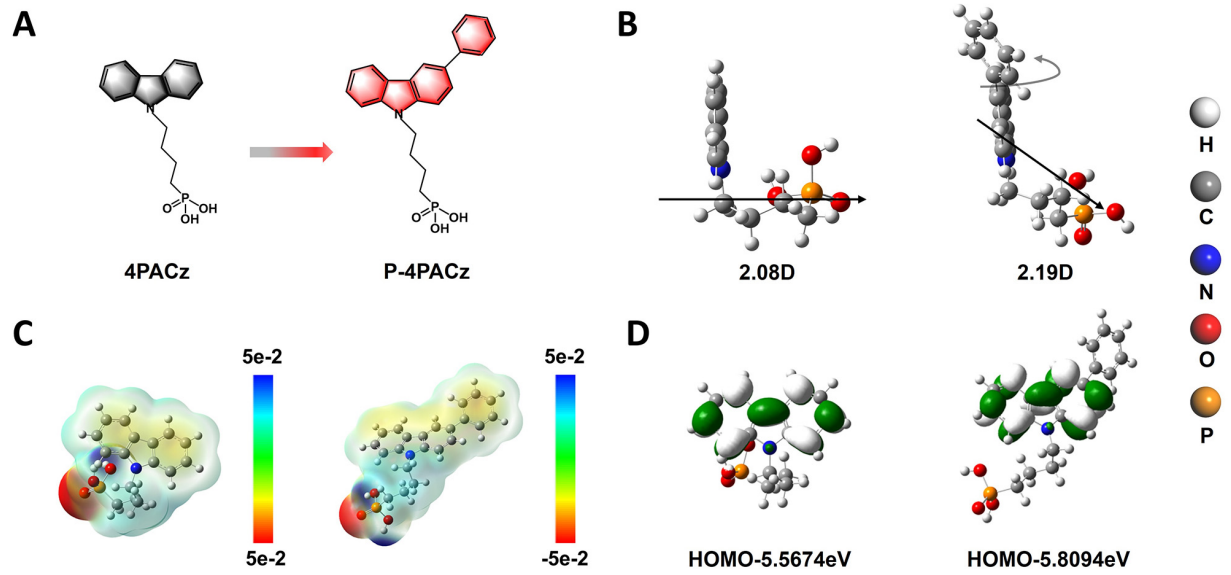

Figure 1. (A) Chemical structures of 4PACz and P-4PACz, (B) dipole moments, (C) Electrostatic Potential distributions, and (D) Highest Occupied Molecular Orbital energy levels of 4PACz and P-4PACz.

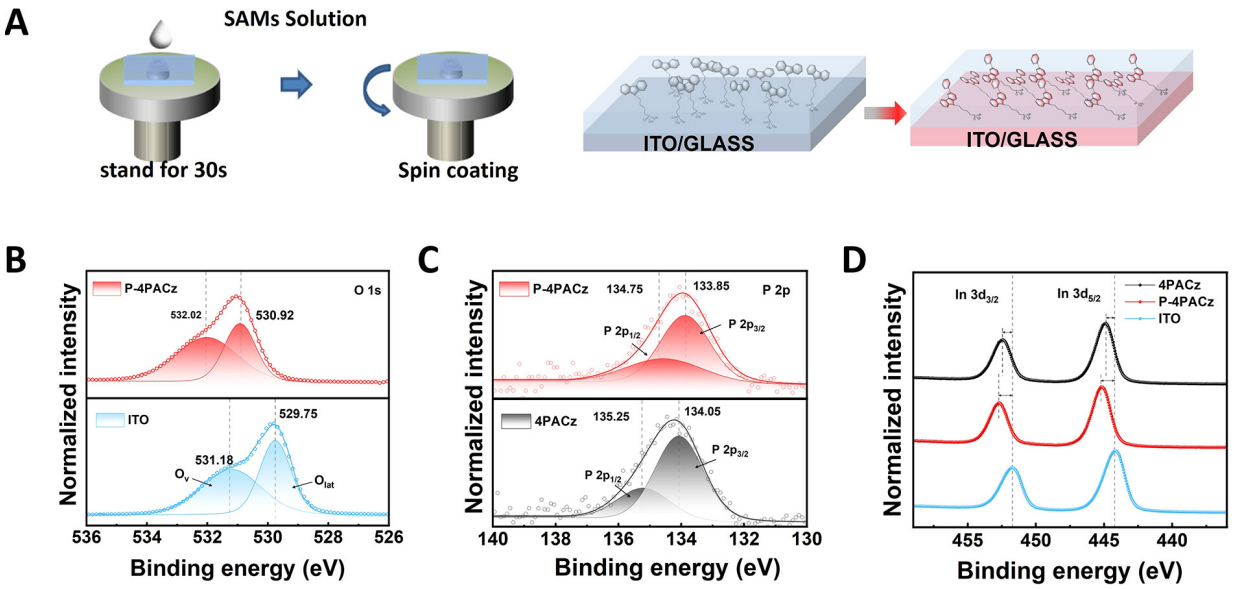

Figure 2. (A) SAM solutions and spin coating processes on ITO substrate, (B) O 1s XPS spectra of bare ITO and ITO/P-4PACz, (C) P 2p XPS spectra of ITO/P-4PACz and ITO/4PACz, (D) In 3d XPS spectra of bare ITO and ITO/SAMs.

Molecular Orbital (HOMO) level in the self-assembled monolayer [Figure 1D]. Specifically, the calculated HOMO levels of 4PACz and P-4PACz are -5.56 and -5.80 eV, respectively, while the corresponding LUMO levels are -0.799 and -0.725 eV [Supplementary Figure 2]. This modulation of frontier molecular orbitals suggests improved energy-level alignment at the interface.

The SAM films (4PACz and P-4PACz) were fabricated on ITO substrates under identical processing conditions (see Experimental Section) to enable a fair comparison of their intrinsic properties [Figure 2A]. UV-vis absorption spectra [Supplementary Figure 3A] show that P-4PACz exhibits nearly identical absorption features to 4PACz, indicating that the asymmetric phenyl substitution does not significantly alter the optical characteristics of the monolayer. Notably, however, the transmittance of the P-4PACz monolayer in the 400-800 nm range is slightly higher than that of both 4PACz and PEDOT:PSS [Supplementary Figure 3B], which is advantageous for maximizing photon utilization in the active layer.

To understand the origin of the improved film morphology of P-4PACz, we first investigated its intrinsic molecular packing and solution-state behavior. Single-crystal structures of the π-scaffolds and full molecules were analyzed. For the pure π-scaffolds, pristine carbazole exhibits a vertical stacking distance of 3.37 Å and a longitudinal slip of 5.73 Å [Supplementary Figure 4A]. In contrast, the 3-phenyl-substituted carbazole shows a substantially shortened vertical distance of 2.47 Å but an increased slip of 6.46 Å [Supplementary Figure 4B], reflecting a shift in the optimal stacking geometry induced by the phenyl substituent. Notably, when the full molecules (including alkyl chains and phosphonic acid groups) are considered, P-4PACz still exhibits a much shorter vertical distance (2.73 Å) compared to 4PACz (3.29 Å) [Supplementary Figure 4C and D], while the slip distances are approximately 6.02 and 5.96 Å, indicating that the π-π stacking is reasonably moderated. This unique stacking mode also influences the solution-state behavior and the film formation of the SAM. As shown in Supplementary Figure 5, at identical concentration (0.5 mg/mL), the 4PACz solution in ethanol exhibits visible turbidity with undissolved particulates, whereas the P-4PACz solution is completely transparent and clear. This difference is also evident in chloroform, a nonpolar solvent, indicating that the superior solubility of P-4PACz is an intrinsic property of its asymmetric molecular structure rather than being solvent-specific. The reduced aggregation tendency in solutions arising from the weakened intermolecular packing in the solid state.

The surface morphologies of bare ITO, ITO/SAMs, and ITO/PEDOT:PSS were characterized by AFM. As shown in Supplementary Figure 6A-D, the ITO/P4PACz exhibits a reduced arithmetic average roughness (Ra = 4.53 nm) compared to bare ITO (Ra = 4.81 nm) and ITO/4PACz (Ra = 4.67 nm), indicating a smoothing effect that is visually supported by the corresponding height profile in Supplementary Figure 6E. In contrast, the SAM-modified surfaces display Ra values similar to that of pristine ITO, which can be attributed to their ultrathin monolayer structure. In contrast, the PEDOT:PSS exhibits a significantly lower Ra value (Ra = 1.89 nm), reflecting its thicker polymeric film that effectively planarizes the underlying ITO surface[36]. Notably, the smoother substrate induced by P4PACz translates into improved activelayer morphology. As shown in Supplementary Figure 7, the PM6:BTPeC9 blend deposited on ITO/P4PACz exhibits a lower surface roughness (Ra = 1.82 nm) compared to that on ITO/4PACz (Ra = 1.99 nm), and approaches that of the PEDOT:PSS reference (Ra = 1.78 nm). This suggests that the P4PACz interlayer not only smooths the ITO surface but also promotes the formation of a more uniform and homogeneous bulk heterojunction film. Surface energy plays a critical role in determining both the efficiency and long-term stability of organic solar cells. To quantify the interfacial wettability, contact angle measurements were conducted using water (H_2O) and formamide (FA) as probe liquids. The water contact angles of ITO/P-4PACz and ITO/4PACz were measured to be 86° and 80°, respectively, significantly higher than that of bare ITO (46°) [Supplementary Figure 8 and 9], indicating enhanced hydrophobicity upon SAM modification. Using the Owens-Wendt-Rabel-Kaelble method, the calculated surface energies of ITO/PEDOT:PSS, ITO/4PACz, and ITO/P-4PACz are 76.7, 40.8, and 38.0 mN m^{-1}, respectively, showing a progressive decrease. Notably, the surface energy of ITO/P-4PACz is closer to that of the active layer PM6:BTP-eC9 (28.9 mN m^{-1}) [Supplementary Table 1], suggesting improved interfacial compatibility. In addition to increased hydrophobicity, this optimized surface energy alignment facilitates better film formation of the active layer, thereby contributing to enhanced device performance.

The formation of SAMs on ITO substrates was confirmed by XPS. The fullspectrum scans of 4PACz and P4PACz [Supplementary Figure 10] showed marked changes in peak intensities relative to bare ITO, indicating successful SAM coverage. Highresolution O 1s corelevel spectra further revealed systematic variations [Figure 2B and Supplementary Figure 11]: the relative area of the component around 531.5 eV, commonly assigned to surface hydroxyl groups or oxygendeficient sites, decreased progressively from 0.95 (bare ITO) to 0.85 (ITO/4PACz) and to 0.65 (ITO/P4PACz). Moreover, the main O 1s peak for ITO/P4PACz exhibited a noticeable positive bindingenergy shift compared to both bare ITO and ITO/4PACz. The changes

suggest that phosphonic acid groups likely consume reactive sites on the ITO surface, thereby contributing to the formation of a more stable interface. Direct evidence for this interfacial bonding is provided by the P 2p spectra [Figure 2C]. Specifically, for P4PACz, the P $2p_{3/2}$ and P $2p_{1/2}$ doublet is observed at 133.85 and 134.75 eV, respectively. Compared with the corresponding peaks of 4PACz (134.05 and 135.25 eV), this represents a systematic negative shift of 0.2-0.5 eV, indicating an increase in electron density around the phosphorus atom in P4PACz upon coordination with the ITO surface. Furthermore, the spectral weight of the lower-binding-energy component (133.85 eV) is more pronounced in P-4PACz, which may reflect an altered distribution of phosphonate binding motifs induced by the asymmetric molecular structure. Furthermore, the In 3d spectra [Figure 2D] reveal that the In $3d_{2/3}$ and In $3d_{5/2}$ peaks of bare ITO are located at 451.725 and 444.225 eV. Upon SAM deposition, these peaks shift to 452.350 and 444.850 eV for 4PACz, and further shift to 452.725 and 445.225 eV for P4PACz. The observed binding energy shifts primarily in the O 1s, P 2p, and In 3d regions collectively indicate an enhanced chemical coupling at the SAM/ITO interface. Notably, the negative shift in the P 2p spectrum suggests increased electron density around the phosphorus atom, consistent with stronger bonding between the phosphonate groups and the ITO substrate. Concurrently, analysis of the C 1s and N 1s spectra [Supplementary Figure 12][37] reveals that the area proportion of the C-P component increased from 19% to 23%. This change reflects an altered electronic environment around the phosphorus center, which is consistent with the P 2p shift and further supports the formation of stronger interfacial interactions.

To further investigate the optoelectronic properties of asymmetric SAM, KPFM measurements were conducted. As shown in Figure 3A and B, ITO/P4PACz exhibits the highest surface potential. The work functions (WFs) of the functionalized ITO substrates were characterized by UPS [Figure 3C and Supplementary Figure 13][38]. The measured WFs for ITO/P4PACz and ITO/4PACz are -5.13 and -5.01 eV, respectively, which aligns with the trend observed in KPFM. The WFs of bare ITO and PEDOT:PSS were determined to be -4.56 and -4.95 eV, respectively, indicating that P4PACz further deepens the WF compared to both 4PACz and PEDOT:PSS[39,40]. This leads to improved energy-level alignment across the interface, thereby enhancing hole extraction and promoting more efficient charge carrier transport.

Local conductivity was characterized by C-AFM under a low bias of 8.7 mV. The average current measured on ITO/P4PACz (4.44 nA) was significantly higher than that on ITO/4PACz (3.77 nA) [Figure 3D and E], suggesting enhanced local charge transport. Considering the smoother morphology observed earlier, this improvement likely reflects that the more uniform and continuous monolayer formed by P-4PACz helps to minimize defects that would otherwise impede current flow. Furthermore, electrical characterization based on sandwich-structured devices showed that the conductivities of 4PACz, P4PACz, and PEDOT:PSS are 1.969×10^{-5}, 2.188×10^{-5}, and 1.364×10^{-5} S·cm^{-1}, respectively [Figure 3F], consistent with the improved current characteristics observed in device performance.

Binary OSCs with the structure ITO/HTLs/PM6:BTPeC9/PNDIT-F3N/Ag were fabricated, with the device architecture and energy level alignment illustrated in Figure 4A and B, respectively[41].

The SAM modification process and optimization conditions for the ITO substrates are detailed in Supplementary Table 2, and the *J-V* curves of the best-performing devices are shown in Figure 4C. The champion device based on 4PACz achieved a PCE of 18.28%, with a J_{SC} of 27.42 mA cm^{-2}, an V_{OC} of 0.865 V, and a fill factor (FF) of 76.54%. In comparison, the champion device employing the optimized P-4PACz as the hole transport layer attained a higher PCE of 19.03%, along with improved J_{SC} (27.87 mA cm^{-2}) and FF (78.86%), based on these values, we find that the improvement in FF from 76.54% to 78.86% contributes dominantly to the overall PCE enhancement. According to the relationship PCE = $V_{OC} \times J_{SC} \times$ FF, the increase in FF accounts for approximately 65% of the total efficiency gain, whereas the contributions from V_{OC} and J_{SC}

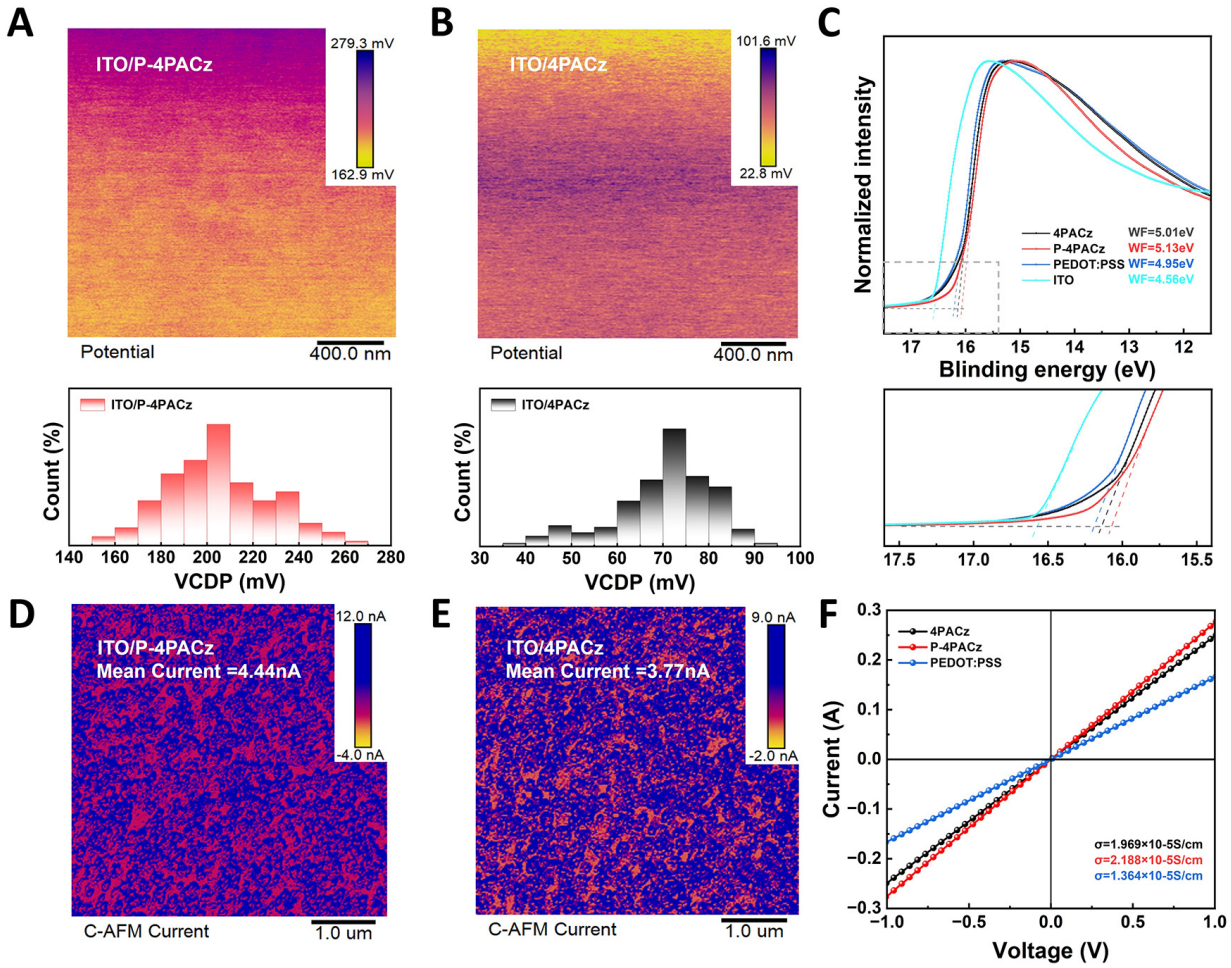

Figure 3. (A and B) Kelvin Probe Force Microscopy images and surface contact potential distributions of ITO/4PACz and ITO/P-4PACz, (C) Ultraviolet Photoelectron Spectroscopy spectra of ITO/HTLs substrates, (D and E) C-AFM images at 8.7 mV, (F) *I-V* characteristics of devices utilizing different HTLs, under an architecture of ITO/HTL/Ag.

are comparatively minor [Supplementary Table 3]. *EQE* spectra of champion devices based on P-4PACz, 4PACz, and PEDOT:PSS are presented in Figure 4D. The integrated J_{SC} values derived from the *EQE* curves are 26.45, 25.90, and 25.00 mA cm^{-2}, respectively. Notably, the champion P-4PACz-based device exhibited significantly higher *EQE* responses in the wavelength ranges of 400-450 nm and 500-800 nm. The dark *J-V* characteristics of the devices are shown in Figure 4E. The P4PACzbased device exhibited a lower current density under both forward and reverse bias, suggesting that the series resistance was reduced and electron injection at the anode interface was more effectively suppressed.

The photovoltaic parameters of devices fabricated with different hole transport layers are statistically summarized in Figure 4F and Supplementary Figure 14. As summarized in Table 1, the P-4PACz-based devices achieved an average PCE of 18.20% (J_{SC} = 27.73 mA cm^{-2}, V_{OC} = 0.866 V, FF = 75.78%), with an average efficiency of 18.20% ± 0.15%, significantly surpassing those of the 4PACz-based (17.52% ± 0.19%) and PEDOT:PSS-based (17.34% ± 0.24%) devices. The performance improvement from 4PACz to P4PACz can be primarily attributed to a notable increase in the FF (from 73.78% ± 0.26% to 75.78% ± 0.25%), accompanied by slight enhancements in both J_{SC} and V_{OC}. These collective enhancements suggest more efficient charge extraction and reduced recombination losses. Furthermore, Supplementary Figure 15 shows that P-4PACz exhibits higher V_{bi} than 4PACz and PEDOT:PSS, which is another key factor contributing to its enhanced

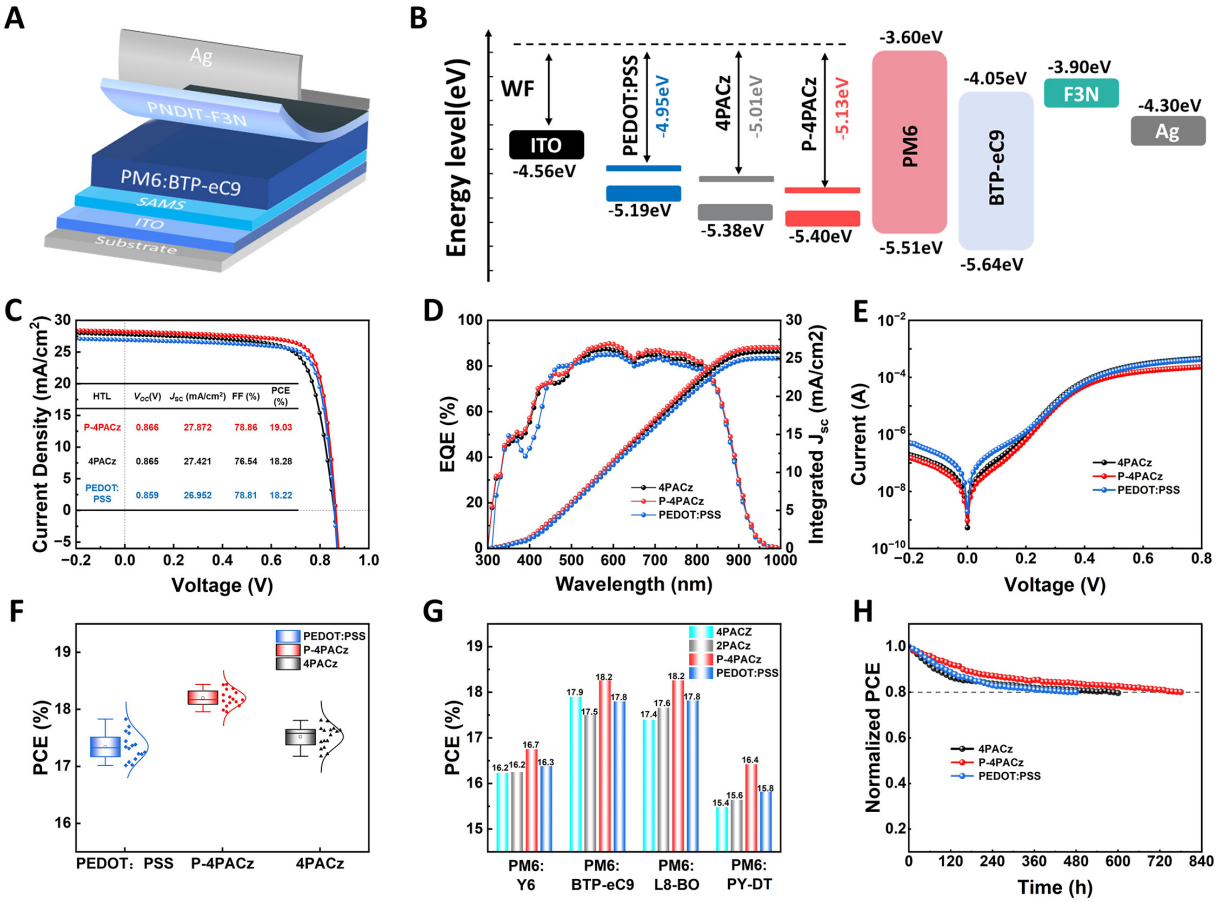

Figure 4. (A) Conventional OSC structure with HTLs, (B) Energy-level alignment among ITO, HTLs, active layer, ETL, and electrodes. (C) *J-V* curves of champion PM6:BTP-eC9 devices with HTLs, (D) *EQE* spectra and integrated J_{SC} of corresponding champion devices, (E) dark *J-V* curves for binary devices, (F) average photovoltaic performance of 16 individual PM6:BTP-eC9-based devices with different HTLs, (G) universality chart of PEDOT and SAMs, and (H) unencapsulated device stability in N_2 (25% RH, 25 °C).

Table 1. Average photovoltaic parameters of different HTL-based OSCs (mean ± SD, *n* = 16)

HTLs	V_{OC} (V)	J_{SC} (mA/cm²)	FF (%)	PCE (%)
4PACz	0.864 ± 0.002	27.47 ± 0.29	73.78 ± 0.26	17.52 ± 0.19
P-4PACz	0.866 ± 0.002	27.73 ± 0.27	75.78 ± 0.25	18.20 ± 0.15
PEDOT:PSS	0.859 ± 0.002	26.61 ± 0.30	75.77 ± 0.34	17.34 ± 0.24

performance. To explore the generality of the asymmetric phosphonic acidbased selfassembled interface, we introduced 4PACz, 2PACz, P4PACz, and PEDOT:PSS into other binary systems (PM6:L8BO, PM6:Y6, and PM6:PYDT, chemical structures shown in Supplementary Figure 16), as illustrated in Figure 4G. The corresponding *J-V* curves are provided in Supplementary Figure 17 and Detailed photovoltaic parameters are summarized in Supplementary Tables 4-6. Importantly, P-4PACz demonstrates universal applicability as an excellent hole-transporting layer across various active layer systems. Unencapsulated devices employing PEDOT:PSS, 4PACz, or P-4PACz as the hole-transport layer were further evaluated under 25 °C, 25% relative humidity, under AM 1.5G illumination (100 mW/cm²); the P-4PACz-based cells delivered the longest *T*80 lifetime, up to 782 h [Figure 4H].

The exciton dissociation and charge collection efficiencies in organic solar cells incorporating different hole-extraction layers were evaluated by analyzing the photocurrent density as a function of effective bias

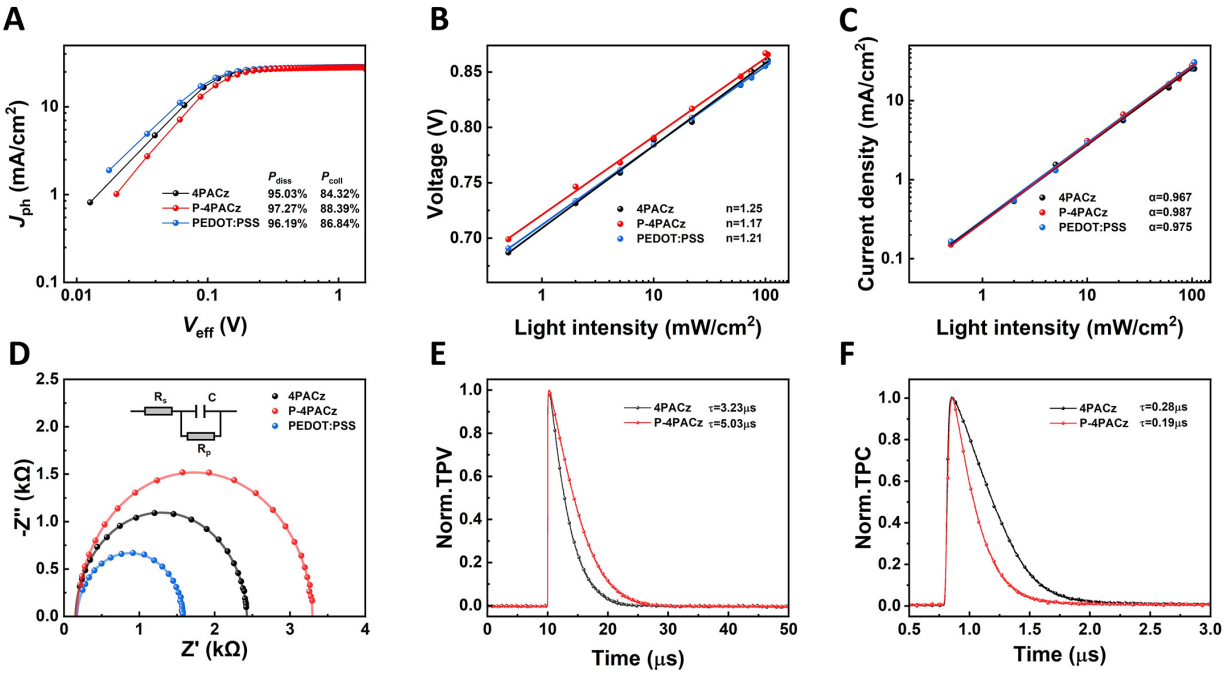

Figure 5. (A) J_{ph}-V_{eff} characteristics for the corresponding devices, (B and C) light-intensity dependence of J_{SC} and V_{OC}, (D) Nyquist plots, (E) transient photovoltage, (F) transient photocurrent decays.

[Figure 5A]. The charge dissociation probability (P_{diss}) and charge collection probability (P_{coll}) are defined as follows: $P_{diss} = J_{ph,SC}/J_{sat}$ and $P_{coll} = J_{ph,MPP}/J_{sat}$, where J_{ph} denotes the photocurrent density and J_{sat} denotes the saturation current density. P_{diss} is typically evaluated under short-circuit conditions and quantifies the efficiency of exciton dissociation into free charge carriers, whereas P_{coll} is evaluated at the maximum power point voltage and reflects the efficiency with which photogenerated free charges are collected by the electrodes. Under short-circuit conditions, the P_{diss} value for devices based on ITO/4PACz, ITO/P-4PACz, and ITO/PEDOT:PSS were 95.03%, 97.27%, and 96.19%, respectively. At the maximum power point, the P_{coll} values were 84.32%, 88.39%, and 86.84%. These results indicate that the device employing P-4PACz exhibits the highest exciton dissociation efficiency.

The trap-assisted recombination behavior was further investigated by examining the semi-logarithmic dependence of V_{OC} on light intensity [Figure 5B]. The fitted slope, expressed in units of n·kT/q, approaches the ideal value of 1 kT/q when trap-assisted recombination is minimal. The device employing P-4PACz exhibits the smallest slope (n = 1.17), which is notably lower than those of the 4PACz-based (n = 1.25) and PEDOT:PSS-based (n = 1.21) devices, indicating more effective suppression of trap-assisted recombination in the P-4PACz-based device. The bimolecular recombination behavior was assessed by analyzing the J_{SC}-P_{light} relationship, described by the power-law dependence $J_{SC} \propto P^{\alpha}$ [Figure 5C]. A value of α closer to unity signifies weaker trap-assisted recombination. As illustrated in Figure 5C, the P-4PACz-based device achieves the highest α value (α = 0.987), surpassing the 4PACz-based (α = 0.967) and PEDOT:PSS-based (α = 0.975) devices, demonstrating more pronounced suppression of bimolecular recombination in the P-4PACz-based device[42,43].

The recombination impedance spectra of different devices appear in Figure 5D. The P4PACzbased device exhibits the highest recombination resistance (1.54 kΩ), significantly exceeding those of the 4PACzbased (1.11 kΩ) and PEDOT:PSSbased devices (0.67 kΩ), indicating more effective suppression of carrier recombination[44]. The P4PACz interlayer can simultaneously optimize energylevel alignment and improve

physical contact at the interface. This synergistic effect not only promotes efficient hole extraction but also substantially reduces carrier recombination losses, thereby contributing to higher FF and PCE. To directly visualize interfacial hole transfer, steady-state PL spectroscopy was performed. The PL intensity of the PM6:BTP-eC9 blend was more effectively quenched on the ITO/P-4PACz substrate compared to ITO/4PACz [Supplementary Figure 18].

Transient photovoltage (TPV) decay measurements show that the carrier lifetime of the device based on P-4PACz (5.03 μs) is longer than that of the device based on 4PACz (3.23 μs), which is consistent with the suppression of trap-assisted non-radiative recombination [Figure 5E]. Transient photocurrent (TPC) analysis further indicates that the charge extraction speed of the device based on P-4PACz is accelerated, as reflected in the reduction of the extraction time from 0.28 to 0.19 μs [Figure 5F]. Holes accumulated rapidly at the 4PACz interface, but the charge extraction efficiency was limited. The asymmetric substitution at the P-4PACz interface improved the alignment mode and the change in work function, forming a more efficient charge extraction channel between the electrode and the active layer. This is also reflected in J_{SC}, ultimately leading to the improvement of the higher PCE of the OSCs.

CONCLUSIONS

In summary, we report an easily accessible asymmetric carbazole-based self-assembled monolayer, P-4PACz, featuring a unilateral phenyl substituent that rationally moderates π-π stacking and enhances dispersion and solubility in solution. The resulting SAM exhibits improved molecular packing, higher conductivity, and lower surface energy, which collectively facilitate better active-layer film formation. Furthermore, the asymmetric design deepens the work function and optimizes energy-level alignment with the donor material, thereby promoting efficient hole extraction and charge transport. These benefits synergistically enhance the open-circuit voltage, short-circuit current density, and particularly the fill factor. This simple yet effective strategy of tailoring intermolecular interactions to optimize film formation offers new insights into the design of SAM materials for organic solar cells.

DECLARATIONS

Authors' contributions

Device fabrication and testing: Yu, Y.; Wang, Z.
Density functional theory calculations: Hong, X.
Material characterization, data validation, methodology design, and critical data curation: Yu, Y.; Hong, X.; Li, Y.
Manuscript drafting and overall coordination: Yu, Y.
Manuscript review, revision, and finalization: Yu, Y.; Hong, X.; Li, Y.; Wang, Z.; Kang, F.; Jiao, Z.; Wei, G.

Availability of data and materials

The data that supports the findings of this study are available from the corresponding author upon reasonable request.

AI and AI-assisted tools Statement

Not applicable.

Financial support and sponsorship

This work was supported by the National Natural Science Foundation of China (Grants No. 52027817 and No. 52471020), and the Tsinghua Shenzhen International Graduate School Overseas Research Cooperation Fund (Grant No. HW2024008).

Conflicts of interest

All authors declared that there are no conflicts of interest.

Ethical approval and consent to participate

Not applicable.

Consent for publication

Not applicable.

Supplementary Materials

Supplementary Materials

REFERENCES

1. Song, W.; Ye, Q.; Chen, Z.; Ge, J.; Xie, L.; Ge, Z. Advances in stretchable organic photovoltaics: flexible transparent electrodes and deformable active layer design. *Adv. Mater.* **2024**, *36*, e2311170. DOI PubMed
2. Ren, J.; Wang, J.; Qiao, J.; et al. Manipulating aggregation kinetics toward efficient all-printed organic solar cells. *Adv. Mater.* **2025**, *37*, e2418353. DOI
3. Brabec, C. J.; Distler, A.; Du, X.; et al. Material strategies to accelerate OPV technology toward a GW technology. *Adv. Energy. Mater.* **2020**, *10*, 2001864. DOI
4. Li, C.; Song, J.; Lai, H.; et al. Non-fullerene acceptors with high crystallinity and photoluminescence quantum yield enable > 20% efficiency organic solar cells. *Nat. Mater.* **2025**, *24*, 433-43. DOI
5. Zhu, L.; Zhang, M.; Zhou, G.; et al. Achieving 20.8% organic solar cells via additive-assisted layer-by-layer fabrication with bulk p-i-n structure and improved optical management. *Joule* **2024**, *8*, 3153-68. DOI
6. Cheng, B.; Xia, X.; Cheng, S.; et al. Precise control over crystallization kinetics by combining nucleating agents and plasticizers for 20.1% efficiency organic solar cells. *Adv. Mater.* **2025**, *37*, e2500357. DOI
7. Li, Q.; Sun, Y.; Yang, C.; et al. Optimizing the component ratio of PEDOT:PSS by water rinse for high efficiency organic solar cells over 16.7. *Sci. Bull.* **2020**, *65*, 747-52. DOI
8. Yang, Q.; Yu, S.; Fu, P.; et al. Boosting performance of non-fullerene organic solar cells by 2D g-C_3N_4 doped PEDOT:PSS. *Adv. Funct. Mater.* **2020**, *30*, 1910205. DOI
9. Yang, X.; Sun, R.; Wang, Y.; et al. Ternary all-polymer solar cells with efficiency up to 18.14% employing a two-step sequential deposition. *Adv. Mater.* **2023**, *35*, e2209350. DOI
10. Jørgensen, M.; Norrman, K.; Krebs, F. C. Stability/degradation of polymer solar cells. *Sol. Energy. Mater. Sol. Cells.* **2008**, *92*, 686-714. DOI
11. Lin, Y.; Firdaus, Y.; Isikgor, F. H.; et al. Self-assembled monolayer enables hole transport layer-free organic solar cells with 18% efficiency and improved operational stability. *ACS. Energy. Lett.* **2020**, *5*, 2935-44. DOI
12. Guan, S.; Li, Y.; Xu, C.; et al. Self-assembled interlayer enables high-performance organic photovoltaics with power conversion efficiency exceeding 20. *Adv. Mater.* **2024**, *36*, e2400342. DOI
13. Fan, B.; Gao, H.; Li, Y.; et al. Integration of polyoxometalate clusters with self-assembled monolayer for efficient and robust organic solar cells. *Joule* **2024**, *8*, 1443-56. DOI
14. Xie, J.; Lin, W.; Zheng, K.; Liang, Z. N-doping donor-dilute semitransparent organic solar cells to weaken donor: acceptor miscibility and consolidate donor-phase continuity. *Adv. Sci.* **2024**, *11*, e2404135. DOI PubMed PMC
15. Chen, Z.; Ge, J.; Song, W.; et al. 20.2% efficiency organic photovoltaics employing a π-extension quinoxaline-based acceptor with ordered arrangement. *Adv. Mater.* **2024**, *36*, e2406690. DOI
16. Azeez, A.; Huang, Y.; Stanly, L.; Kan, Z.; Karuthedath, S. Advances in self-assembled monolayer-engineered organic solar cells. *EES. Sol.* **2025**, *1*, 248-66. DOI
17. Chen, Q.; Sun, K.; Franco, L. R.; et al. Effects of alkyl spacer length in carbazole-based self-assembled monolayer materials on molecular conformation and organic solar cell performance. *Adv. Sci.* **2025**, *12*, e2410277. DOI PubMed PMC
18. Lee, M. J.; Park, J.; Kim, T. H.; Saeed, M. A.; Lee, G. M.; Shim, J. W. Tailoring hole-selective contacts via self-assembled monolayers for advancing indoor organic photovoltaic and capacitor devices. *Chem. Eng. J.* **2024**, *481*, 148481. DOI
19. Li, M.; Li, Z.; Fu, H.; et al. Molecularly engineered self-assembled monolayers as effective hole-selective layers for organic solar cells. *ACS. Appl. Energy. Mater.* **2024**, *7*, 1306-12. DOI
20. Lin, Y.; Zhang, Y.; Zhang, J.; et al. 18.9% efficient organic solar cells based on n-doped bulk-heterojunction and halogen-substituted self-assembled monolayers as hole extracting interlayers. *Adv. Energy. Mater.* **2022**, *12*, 2202503. DOI

21. Geng, R.; Gao, S.; Liu, J.; et al. Tunning interfacial interaction strategy by asymmetric configuration to construct self-assembly materials for efficient organic solar cells. *Chem. Eng. J.* **2024**, *483*, 149035. DOI
22. Chen, Q.; Wu, J.; Gumbo, M.; et al. Organic solar cells with 20.12% efficiency enabled by monosubstituted carbazole-based self-assembled monolayers. *ACS. Energy. Lett.* **2025**, *10*, 5584-95. DOI
23. Du, Y.; Zhao, Q.; Yuan, Q.; et al. Boosting the dipole effect of self-assembled monolayers via an asymmetric sulfur functionalization strategy. *ACS. Appl. Energy. Mater.* **2025**, *8*, 12294-302. DOI
24. Liu, L.; Yu, F.; Hu, D.; et al. Breaking the symmetry of interfacial molecules with push-pull substituents enables 19.67% efficiency organic solar cells featuring enhanced charge extraction. *Energy. Environ. Sci.* **2025**, *18*, 1722-31. DOI
25. Guo, C.; Du, H. Q.; Wang, Y. C.; et al. Bifacially reinforced self-assembled monolayer interfaces for minimized recombination loss and enhanced stability in perovskite/silicon tandem solar cells. *Adv. Mater.* **2025**, *37*, e2504520. DOI
26. Yu, X.; Ding, P.; Yang, D.; et al. Self-assembled molecules with asymmetric backbone for highly stable binary organic solar cells with 19.7% efficiency. *Angew. Chem. Int. Ed.* **2024**, *63*, e202401518. DOI
27. Wang, W.; Liu, X.; Wang, J.; et al. Versatile self-assembled molecule enables high-efficiency wide-bandgap perovskite solar cells and organic solar cells. *Adv. Energy. Mater.* **2023**, *13*, 2300694. DOI
28. Sun, X.; Zhang, C.; Yao, Y.; et al. 19.35% efficient binary bulk-heterojunction organic photovoltaic enabled by optimizing bromine-substituted self-assembled carbazole based molecules. *Adv. Funct. Mater.* **2024**, *34*, 2406060. DOI
29. Fei, C.; Kuvayskaya, A.; Huskie, T.; et al. Phosphonic acid group positions dependent face-on and edge-on configurations in carbazole-based SAMs and impacts on perovskite solar cell performance. *ACS. Energy. Lett.* **2025**, *10*, 5192-8. DOI
30. Kong, Y.; Wang, W.; Guo, X.; et al. Decoding the role of molecular orientation in conjugated self-assembled monolayers for high-performance binary organic photovoltaics approaching 20% efficiency. *Adv. Mater.* **2025**, *37*, e2501117. DOI
31. Lenaers, S.; Lammar, S.; Krishna, A.; et al. Pyrene-based self-assembled monolayer with improved surface coverage and energy level alignment for perovskite solar cells. *Adv. Funct. Mater.* **2024**, *36*, 2411922. DOI
32. Sun, X.; Wang, F.; Yang, G.; et al. From 20% single-junction organic photovoltaics to 26% perovskite/organic tandem solar cells: self-assembled hole transport molecules matter. *Energy. Environ. Sci.* **2025**, *18*, 2536-45. DOI
33. Tan, Q.; Wang, H.; Tang, S.; et al. Asymmetric dimethyl-indenocarbazole phosphonic acid molecules with expanded π-conjugation for inverted perovskite solar cells. *Adv. Funct. Mater.* **2025**, *35*, 2501147. DOI
34. Bin, H.; Datta, K.; Wang, J.; et al. Finetuning hole-extracting monolayers for efficient organic solar cells. *ACS. Appl. Mater. Interfaces.* **2022**, *14*, 16497-504. DOI PubMed PMC
35. Duan, W.; Chen, K.; Pi, B.; et al. A spatial structure regulation strategy modulated the solubility and compactness of novel face-on oriented bisphosphonate-anchored SAMs for efficient inverted perovskite solar cells. *Energy. Environ. Sci.* **2025**, *18*, 7231-44. DOI
36. Shafe, A. A.; Raza, S.; Henry, R.; Liu, J.; O'connor, B. T. Improving adhesion in organic photovoltaic cells with self-assembled monolayers. *ACS. Energy. Lett.* **2025**, *10*, 1865-73. DOI
37. Zhang, N.; Jiang, W.; An, Y.; et al. Enhancing UV stability and charge extraction in organic solar cells with phenyl-linked aromatic self-assembled monolayer. *Adv. Funct. Mater.* **2025**, *35*, 2423178. DOI
38. Jiang, H.; Liang, Q.; Guo, H.; et al. All roads lead to rome: isomers with divergent cathode modification mechanisms toward ohmic contact. *J. Am. Chem. Soc.* **2024**, *146*, 30262-71. DOI
39. Lange, I.; Reiter, S.; Pätzel, M.; et al. Tuning the work function of polar zinc oxide surfaces using modified phosphonic acid self-assembled monolayers. *Adv. Funct. Mater.* **2014**, *24*, 7014-24. DOI
40. Singh, N.; Mohapatra, A.; Chu, C.; Tao, Y. Modulation of work function of ITO by self-assembled monolayer and its effect on device characteristics of inverted perovskite solar cells. *Org. Electron.* **2021**, *98*, 106297. DOI
41. Liu, H.; Gao, X.; Xin, Y.; et al. Central fluorination strategy of biphosphonic acid molecule for self-assembled monolayer enables efficient organic solar cells. *Sci. China. Mater.* **2025**, *68*, 1408-14. DOI
42. Wu, J.; Li, G.; Fang, J.; et al. Random terpolymer based on thiophene-thiazolothiazole unit enabling efficient non-fullerene organic solar cells. *Nat. Commun.* **2020**, *11*, 4612. DOI PubMed PMC
43. Wu, J.; Sun, F.; Hua, F.; et al. Balance processing and molecular packing via structural disordering in a random terpolymer for over 19% efficiency non-halogenated solvent organic solar cells. *Adv. Energy. Mater.* **2025**, *15*, 2500024. DOI
44. Fabregat-Santiago, F.; Garcia-Belmonte, G.; Mora-Seró, I.; Bisquert, J. Characterization of nanostructured hybrid and organic solar cells by impedance spectroscopy. *Phys. Chem. Chem. Phys.* **2011**, *13*, 9083-118. DOI PubMed